Construction and Building Materials 449 (2024) 138250

Contents lists available at ScienceDirect

Construction and Building Materials

journal homepage: www.elsevier.com/locate/conbuildmat

A theoretical model for the load-transfer analyses of load distributive compression anchor integrating DSC-based interface nonlinear model

Shimin Zhu [a,*,1], Changfu Chen [b,2], Genbao Zhang [c], Mingbin Wang [a], Zhuangwei Zhang [a]

[a] School of Hydraulic and Civil Engineering, Ludong University, Yantai, Shandong 264025, China
[b] College of Civil Engineering, Hunan University, Changsha, Hunan 410082, China
[c] College of Civil Engineering, Hunan City University, Yiyang, Hunan 413000, China

ARTICLE INFO

Keywords:
Load distributive compression anchor
Soil-anchor interface
Load-transfer behavior
Theoretical modeling

ABSTRACT

An innovative anchorage technology named load distributive compression anchor (LDCA) has recently been employed in a multitude of geotechnical engineering. The anchoring structure comprises multiple anchor bodies, thereby overcoming the bearing defects associated with conventional load-concentrated anchors and providing superior bearing performance. The complex structural configuration of LDCA considerably complicates the process of load-transfer theoretical modeling. A lack of relevant studies from theoretical solution perspective is yet evident in previous works. In this paper, a theoretical model was proposed for the load-transfer analyses of LDCA, of which the soil-anchor interface mechanical behavior was specially characterized by a disturbed state concept (DSC)-based nonlinear model. The mechanical simulation for the connections in different anchor bodies was incorporated into the theoretical analysis framework through the utilization of finite difference method. Three groups of 3D finite element (FE) models were established to simulate the load-transfer behaviors of LDCAs with different numbers of anchor bodies. The theoretical calculations agree well with the FE numerical results and the in-situ pullout test data, thereby confirming the applicability of the load-transfer theoretical model. The axial force and interface shear stress distributions, as well as the bearing capacity for LDCAs, were discussed based on theoretical calculations and FE simulations. Sensitivity analysis of several key design parameters was conducted to investigate their effects on the bearing capacity of LDCAs. The findings achieved in this study can provide insights into the understanding of the load-transfer behaviors of LDCA, and contribute to the bearing performance evaluation.

1. Introduction

The anchorage technology has widespread applications in a variety of geotechnical engineering, such as deep excavations, slopes, tunnels, and retaining walls, which benefits from its merits of convenient construction, low cost, good bearing performance, etc [1,2]. Ground anchors are generally provided with a relatively long anchorage segment. The pullout load subjected to the anchor is transferred to the surrounding stable geomaterial mass through interface shear resistance. An inevitable consequence of the interaction between the anchors and the surrounding soil or rock is the emergence of load-transfer problem for the structure. This has become the prevailing view among industry experts [3,4]. The load-transfer behavior of the anchors exerts a controlling influence on the bearing performance of anchorage structure. Therefore, a thorough comprehension of the load-transfer behavior of the anchors is of great importance to the design practice and performance assessment of anchorage system.

The earliest anchorage technology employed in geotechnical engineering was load-concentrated anchor. This technology is comprised of two distinct types: tension-concentrated anchor and pressure-concentrated anchor [5]. The results of numerous tests [6–8] and theoretical analyses [9–13] attest to the fact that the anchorage length capable of exerting interface shear resistance is restricted for the load-concentrated anchors [14]. In other words, there exists an effective

* Corresponding author.
E-mail addresses: smzhu@ldu.edu.cn (S. Zhu), cfchen@hnu.edu.cn (C. Chen), genbao@hncu.edu.cn (G. Zhang), wangmingbin@ldu.edu.cn (M. Wang), ZZW13215554663@163.com (Z. Zhang).
[1] ORCID: https://orcid.org/0000-0002-7464-8227
[2] ORCID: https://orcid.org/0000-0002-4800-5615

https://doi.org/10.1016/j.conbuildmat.2024.138250
Received 24 July 2024; Received in revised form 30 August 2024; Accepted 5 September 2024

anchorage length for this type of anchor. The underlying cause of this issue can be attributed to the concentrated distribution of axial stress at the anchor head, coupled with an uneven distribution of interface shear stress along the bond length. The longer the anchorage segment, the more significant the uneven stress distribution. There will be a negligible increase in bearing capacity for load-concentrated anchors if the anchorage segment exceeds the effective anchorage length. Therefore, an excessive anchorage length for load-concentrated anchor is unadvisable and should be avoided in engineering practice, which is actually stipulated in relevant design criteria [15,16]. The effective anchorage length for load-concentrated anchor is dependent on the physical and mechanical properties of the surrounding soil or rock. Specifically, the effective anchorage length is shorter in instances where the geomaterial mass equips with a greater strength [9]. Such an outcome is attributable to the greater interface shear resistance. A shorter anchorage length will result in a greater average interface shear stress, which is conducive to the sufficient mobilization of interface shear resistance. However, if the anchorage length is designed to be insufficient, the bearing capacity of the anchors may be unable to fulfill the engineering requirements.

Load distributive compression anchor (LDCA) was invented in recent years. The objective of developing LDCA is to overcome the bearing defects associated with load-concentrated anchors, thereby offering enhanced bearing performance [17–19]. The anchorage segment for LDCA comprises multiple anchor bodies, the structural configuration of which is illustrated in Fig. 1. The entire anchorage length is the sum of the length of each anchor body. The pullout load exerted on the anchor head can be converted into several compressive forces through the appropriate mechanical connections. The dispersion of pullout load effectively eliminates stress concentration and facilitates a more uniform distribution of interface shear stress. The anchor bodies are predominantly compressed for LDCA, which exhibits similarities to compression-type anchors [20]. Accordingly, the surrounding geomaterial mass is subjected to compression as a result of the radial expansion of anchor bodies, which is actually a form of the Poisson effect. This phenomenon further leads to the increments of interface normal stress and interface shear strength [21]. To summarize, the bearing performance of LDCA is superior to that of load-concentrated anchor, but its more complex structural configuration considerably complicates the load-transfer mechanism.

In recent years, a series of in-situ pullout tests were conducted by various scholars with the aim of investigating the influence of the interval and number of anchor bodies on the bearing performance and load-transfer behaviors of LDCA [18,22–24]. Furthermore, the stress distributions of LDCA were also analyzed by the implementation of finite element numerical simulation [25–27] and analytical modeling [25–27]. Hereinto, there are some typical relevant achievements in analytical analysis. Rui et al. [28] summarized the distribution forms of interface shear stress over anchorage segment and proposed a corresponding analysis method. He et al. [29] exploited an analytical model for the load-transfer behavior of compression-type anchors, wherein the interaction between soil and anchor was characterized by an elastic model. Zhu et al. [30] established a theoretical model that can predict the stress distribution and the bearing capacity of recoverable anchors embedded in layer soils. In fact, the aforementioned compression-type anchors and recoverable anchors can both be classified within the category of load-concentrated anchors. It can be seen from the above analysis that the theoretical research was mainly aimed at load-concentrated anchors, yet few studies for LDCA. As evidenced by the preceding analysis, the majority of theoretical researches in this field were focused on load-concentrated anchors, yet a notable dearth of studies is dedicated to LDCA. Two issues should be addressed prior to the implementation of load-transfer theoretical modeling for LDCA, which includes the characterization of the intricate soil-anchor interface behaviors as well as the mechanical simulation for the connections in different anchor bodies. Among that, a nonlinear interface mechanical model capable of reflecting the effect of normal stress is a fundamental necessity for the former. These two issues considerably complicate the process of load-transfer theoretical modeling for LDCA, and the subject is still less studied in reported works.

In this paper, a theoretical model was proposed for the load-transfer analyses of LDCA. A disturbed state concept (DSC)-based nonlinear model was employed to characterize the soil-anchor interface mechanical behavior, with consideration given to the interface normal stress. The mechanical simulation for the connections in different anchor

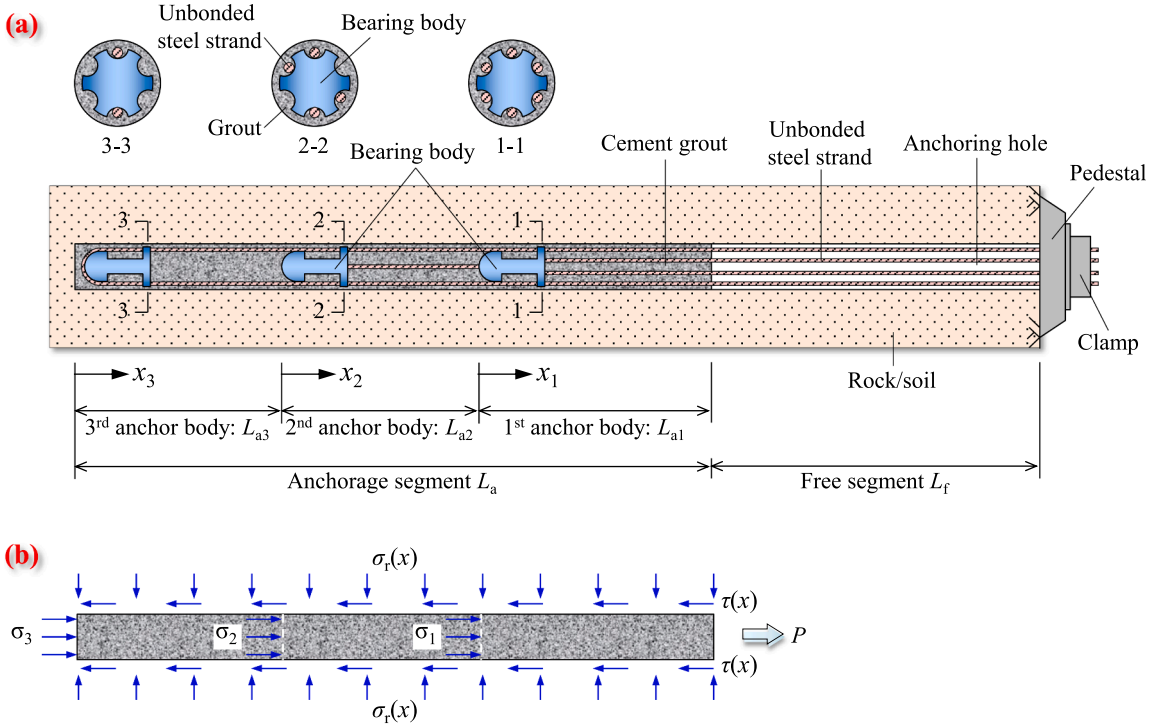

Fig. 1. Structural and mechanical characteristics of LDCA: (a) structure and component; (b) load-transfer mechanism.

bodies was specially incorporated into the analysis framework through the utilization of finite difference method. The load-transfer behaviors for three groups of LDCAs with different numbers of anchor bodies were investigated via three-dimensional finite element (FE) simulation. The FE numerical results and two groups of in-situ pullout test data for LDCAs were used to examine the availability of the load-transfer theoretical model. The axial force and interface shear stress distributions, as well as the bearing capacity for LDCAs, were discussed based on theoretical calculations and FE simulations. Parametric studies were finally conducted to evaluate the effects of some key design parameters on the bearing capacity of LDCA.

2. Bearing mechanism of LDCA

There are multiple bearing bodies in anchorage segment for LDCA. All bearing bodies are jointed with anchor head by dispersive unbonded steel strands. The pullout load applied on the anchor head can thus be converted into several compressive forces through this mechanical connection, which are distributed to different positions in the anchorage segment. Fig. 1 illustrates the structural and mechanical characteristics of LDCA with three anchor bodies. The special case is utilized as an example to explain the bearing mechanism of LDCA. The total pullout load P is dispersed by unbonded steel strands into three loads P_1, P_2, and P_3 that are applied on the 1st, 2nd, and 3rd bearing bodies, respectively. Noteworthy that the total pullout load is equal to the sum of all individual loads. The three individual loads will further be transferred and converted into three compressive stresses σ_1, σ_2, and σ_3 applied on the cement grout bodies in contact with the bearing plates. As a result, the grouted bodies will work in three-dimensional compressive stress state. The soil or rock surrounding the anchor can be inferred to be compressed as well due to the radial expansion of grout body. That is actually the Poisson effect and will lead to the increment of normal stress over the soil-grout interface [30]. Ulteriorly, it improves the soil-grout interface shear strength, thereby enhancing the bearing performance of LDCA. In addition, the pullout load separation for LDCA can almost eliminate stress concentration. The soil-grout interface shear stress tends to a more uniform distribution along the anchorage segment. Hence, compared with the load-concentrated anchor, LDCA is equipped with a greater pullout capacity.

Several scattered compressive forces are exerted on the contact surface between grout and bearing plate for LDCA, including cross Sections 1–1, 2–2, and 3–3 in Fig. 1. As a consequence, the axial stress of anchor changes abruptly at these cross sections, and exhibits the piecewise form for the stress distribution along the anchorage segment. The impacts from different compressive forces will be superimposed on the stress distribution of each anchor body [25], which is similar to the group pile or anchor effect. For example, compressive stress σ_1 not only affects 1st anchor body but also the adjacent 2nd anchor body, as shown in Fig. 2. If the interval between adjacent bearing bodies is narrow, that is, the anchor body is short in length, the compressive force subjected to each anchor body cannot be fully dissipated, so that the residual force is transferred to the next anchor body. It is reflected by a larger axial stress of anchor body than the applied compressive stress (Fig. 2a). In the event that the interval is wide, tensile stress will exist in the anchor body as a consequence of the traction derived from the movement of the bearing body. Concomitant with this is small axial stress, which is less than the applied compressive stress at the head of the anchor body (Fig. 2b). It can be obviously deduced that the dispersion of pullout load for LDCA exacerbates the complexity of the load-transfer problem and heightens the difficulty in theoretical analysis.

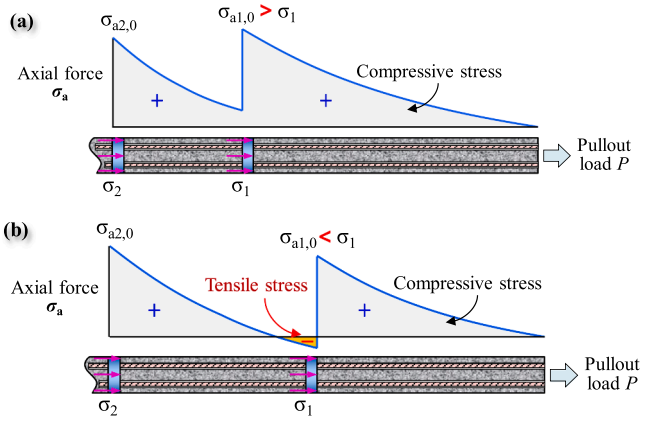

Fig. 2. Schematic drawing of stress overlap phenomenon for different anchor bodies: (a) narrow bearing body interval; (b) wide bearing body interval.

3. A theoretical model for the load-transfer analyses of LDCA

3.1. Basic assumptions

The anchor bodies of LDCA are capable of functioning in compressive stress state, which results in the compression of the surrounding soil and rock. The soil-anchor interface normal stress is inevitably increased during this process. This is markedly distinct from the conventional tension-type anchors. Hence, an interface constitutive model equipped with the capacity to characterize the nonlinear behaviors exhibited by the soil-anchor interface, as well as to reflect the effect of normal stress, is imperatively fundamental to the load-transfer theoretical modeling of LDCA. Meanwhile, as mentioned above, the decentralization of pullout load for LDCA complicates its load-transfer behaviors, thereby heightening the challenge of theoretical analysis. The following assumptions are suggested specially to facilitate theoretical modeling.

(a) The anchor bodies and the surrounding soil are all in elastic state, and their stress-strain responses obey Hooke's law.
(b) The unbonded steel strands are very small in diameter compared to the anchor body. Hence, the holes in cement grout where the steel strands are located are ignored. That is, the anchor body is assumed to be a uniform cylinder.
(c) All anchor bodies do not disengage to remain as a whole during pullout loading. The pullout displacement or the soil-anchor interface shear displacement is equal and continuous at the both ends of bearing body.
(d) Neglecting the difference in diameter between the bearing plate and the anchor hole. The dispersed compressive forces transferred from the bearing plates are exerted uniformly over the entire cross-sections of each head of anchor bodies.
(e) The compressive forces applied on different anchor bodies increase in a constant proportion. It can be expressed as:

$$[P_1, P_2, \cdots, P_{n-1}, P_n]^T = P_n[\alpha_1, \alpha_2, \cdots, \alpha_{n-1}, 1]^T \quad (1)$$

where, α_i (i=1,…, n-1) represents the proportional coefficient of compressive force exerted on the i^{th} and n^{th} anchor bodies. The value of α_i can be defined according to loading requirements.

Based on the above five assumptions, the load-transfer behavior of LDCA was modelled theoretically as follows.

3.2. Load-transfer theoretical modeling

As illustrated in Fig. 1, the LDCA is L_a in in total anchorage length, L_f in free length. There are n anchor bodies, of which the i^{th} anchor body is L_{ai} in length. Local coordinate systems x_i ($0 \leq x_i \leq L_{ai}$) were established with the bottom surface of each bearing plate as the coordinate origin. A random micro-segment from the i^{th} anchor body was selected for analyzing the stress-deformation responses of LDCA (see Fig. 3). All basic equations used in the load-transfer theoretical modeling were determined below.

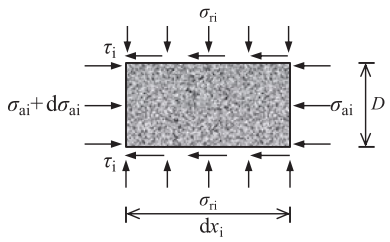

Fig. 3. Stress distribution in a micro-segment from the i^{th} anchor body with length of dx_i.

Deformation equation: according to assumptions (a) and (b), the relation between axial strain and triaxial stress of the anchor body can be expressed as:

$$\varepsilon_{ai}(x_i) = \frac{1}{E_g}\left\{\sigma_{ai}(x_i) - \nu_g\left[\sigma_{yi}(x_i) + \sigma_{zi}(x_i)\right]\right\} \tag{2}$$

where, $\varepsilon_{ai}(x_i)$ represents the axial strain of anchor body; $\sigma_{ai}(x_i)$ represents the axial stress; $\sigma_{yi}(x_i)$ and $\sigma_{zi}(x_i)$ represent the normal stresses along y and z directions, respectively; E_g and ν_g represent Young's modulus and Poisson's ratio of the anchor body, respectively.

Because $\sigma_{yi}(x_i)$=$\sigma_{zi}(x_i)$ =$\sigma_{ri}(x_i)$ for ground anchors, Eq. (2) can be transformed into the following form:

$$\varepsilon_{ai}(x_i) = \frac{1}{E_g}\left[\sigma_{ai}(x_i) - 2\nu_g\sigma_{ri}(x_i)\right] \tag{3}$$

where, $\sigma_{ri}(x_i)$ is the soil-anchor interface normal stress.

Meanwhile, in reference to Hooke's law, the radial expansion strain of anchor body $\varepsilon_{ri}(x_i)$ can be determined as:

$$\varepsilon_{ri}(x_i) = \frac{1}{E_g}\left[\nu_g\sigma_{ai}(x_i) + (\nu_g - 1)\sigma_{ri}(x_i)\right] \tag{4}$$

According to cavity expansion theory and assumption (a), the radial compressive strain of the surrounding soil $\varepsilon_{si}(x_i, r_i)$ can be deduced as:

$$\varepsilon_{si}(x_i, r_i) = \frac{(1+\nu_s)}{E_s}\frac{{r_0}^2}{{r_i}^2}\sigma_{ri}(x_i) \tag{5}$$

where, ν_s and E_s are Poisson's ratio and Young's modulus of the surrounding soil, respectively; r_0 is the radius of anchor body; r_i represents the displacement from the center of the anchor hole.

The radial expansion deformation of anchor bodies should be in harmony with their surrounding soil at the contacted interface (r_i=r_0) when the scattered compressive forces come into play. Hence, Eq. (6) can be deduced by combining Eqs. (4) and (5).

$$\sigma_{ri}(x_i) = k\cdot\sigma_{ai}(x_i) \tag{6}$$

where, $k = \frac{\nu_g E_s}{E_g(1+\nu_s)+E_s(1-\nu_g)}$.

Eq. (6) describes the relationship between the axial stress of anchor body and the soil-anchor interface normal stress. Noteworthy that this equation is applicable only when the anchor body is under compressive state. The interface normal stress should be zero if the anchor body is in tension state. The relationship between $\sigma_{ri}(x_i)$ and $\sigma_{ai}(x_i)$ can thus be updated as:

$$\sigma_{ri}(x_i) = f(\sigma_{ai}) = \begin{cases} 0, \sigma_{ai}(x_i) < 0 \\ k\cdot\sigma_{ai}(x_i), \sigma_{ai}(x_i) \geq 0 \end{cases} \tag{7}$$

Geometric equation: the axial deformation of the anchor body micro-segment is equal to the difference of interface shear displacement or pullout displacement at its both ends. Hence, geometric equation can be expressed in the form of Eq. (8).

$$\varepsilon_{ai}(x_i) = -\frac{ds_i(x_i)}{dx_i} \tag{8}$$

where, $s_i(x_i)$ represents the soil-anchor interface shear displacement.

Force equilibrium equation can be derived according to Fig. 3, as shown below.

$$\frac{d\sigma_{ai}(x_i)}{dx_i} + \frac{u_p}{A_g}\tau_i(x_i) = 0 \tag{9}$$

Where, A_g and u_p represent the cross-sectional area and the perimeter of anchor body; $\tau_i(x_i)$ represents the soil-anchor interface shear stress.

The load-transfer governing equation of LDCA can be derived by incorporating Eqs. (3), (7), (8), and (9), as described in Eq. (10).

$$\frac{d^2 s_i(x_i)}{dx_i^2} + \frac{\mu_p\tau_i(s_i)}{E_g A_g}\cdot\left[2\nu_g\frac{df(\sigma_{ai})}{d\sigma_{ai}} - 1\right] = 0 \tag{10}$$

The governing equation should satisfy the following two boundary conditions.

(a) At the head (x_1=L_{a1}) and the toe (x_n=0) of the total anchorage segment (see Fig. 1):

$$\begin{cases} x_1 = L_{a1} : \sigma_{a1,L_{a1}} = 0 \\ x_n = 0 : \sigma_{an,0} = \sigma_n = \dfrac{P_n}{A_g} \end{cases} \tag{11}$$

where, $\sigma_{a1,La1}$ and $\sigma_{an,0}$ are the axial stresses of anchor body at the head and toe, respectively; P_n is the compressive force subjected to the n^{th} anchor body.

(b) At the positions of the interior bearing plate (i=1,…, n-1): as illustrated in Fig. 4, the anchor bodies before and after the bearing plate should meet the stress conditions represented in Eq. (12).

$$\sigma_{ai,0} - \sigma_{a(i+1),L_{a(i+1)}} = \sigma_i = \frac{P_i}{A_g} = \frac{\alpha_i P_n}{A_g} \tag{12}$$

where, $\sigma_{ai,0}$ is the axial stress of the i^{th} anchor body at initial position (x_i=0); $\sigma_{a(i+1),L_{a(i+1)}}$ is the axial stress of the i+1th anchor body at terminal

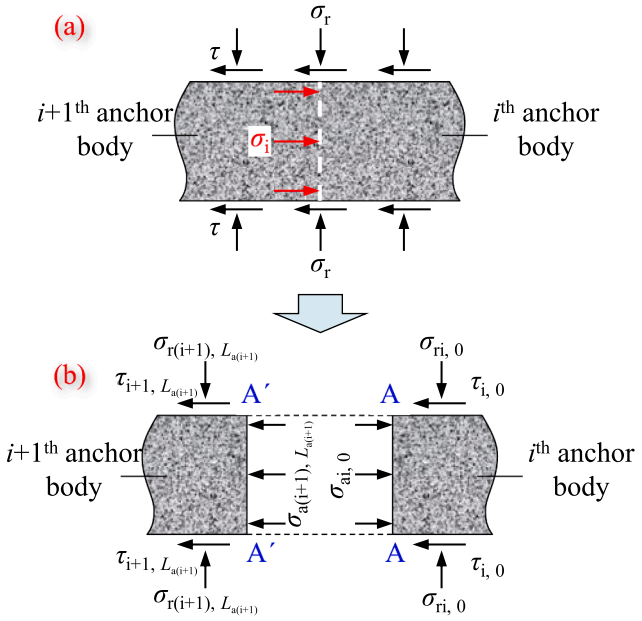

Fig. 4. Stress state of the anchor body at bearing plate: (a) actual stress state; (b) simplified stress state for theoretical modeling.

position (x_{i+1}=$L_{a(i+1)}$); α_i is the proportional coefficient of compressive force exerted on the i^{th} and n^{th} anchor bodies.

There are three variables in Eq. (10), which include soil-anchor interface shear stress $\tau_i(x_i)$, interface shear displacement $s_i(x_i)$ and axial stress $\sigma_{ai}(x_i)$. Hereinto, $\sigma_{ai}(x_i)$ is related to the interface normal stress $\sigma_{ri}(x_i)$, as derived in Eq. (7). The key to solving the load-transfer governing equation is to find a suitable model to characterize the relationship between these three variables. Therefore, an interface nonlinear model considering the effect of interface normal stress is inevitable.

3.3. DSC-based interface nonlinear model

As aforementioned, an interface shear model that can consider the effect of normal stress is fundamental to the load-transfer analysis of LDCA. The disturbed state concept (DSC) theory provides an applicable and appropriate modeling method for characterizing the complex interface shear behaviors [31,32]. An interface nonlinear model was specially developed based on DSC theory, the structure of which was illustrated in Fig. 5. The basic form of this model is as follows:

$$\tau = (1-D)\tau_a + D\tau_c \tag{13}$$

where, τ represents the actual interface shear stress; τ_a represents the shear stress sustained by relative intact (RI) state interface elements; τ_c represents the shear stress sustained by fully adjusted (FA) state interface elements; D is the disturbance function.

As shown in Fig. 5, when the interface shear stress τ is small, it exerts a comparatively minimal influence on the anchor-soil interface, thereby reducing the disturbance. Consequently, the disturbance function D tends towards a relatively small value. The interface shear strength is predominantly attributable to the RI state interface elements. This is reflected in the regularity that the observed τ-s curve is in close approximation with that of RI state. Meanwhile, as the increase of interface shear stress τ, the pullout load exerts a greater influence, resulting in a corresponding increase of the interface elements in FA state as well as the disturbance factor D. Once the interface shear stress τ exceeds interface shear strength, the observed τ-s curve will show the softened form and gradually approach the FA state.

It is extremely crucial to select or develop suitable models to characterize the RI and FA state responses. In this interface model, hyperbolic model and Mohr-Coulomb failure criteria were adopted to simulate the mechanical responses of soil-anchor interface in RI and FA states, respectively. Disturbance function D could be established by describing the strength of all interface elements using Weibull distribution. The DSC-based interface nonlinear model can be derived, as shown in Eq. (14). More details can be found in the studies from Zhu et al. [30].

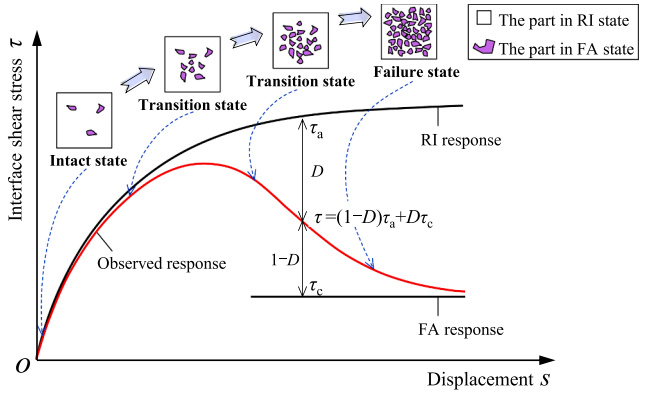

Fig. 5. Schematic of the DSC-based interface nonlinear model and the evolution of interface elements.

$$\tau = \exp\left[-\left(\frac{s}{\xi}\right)^{\eta}\right]\cdot\frac{s}{s_{cr}+s}(\sigma_r \tan\varphi_i + c_i) + \left\{1-\exp\left[-\left(\frac{s}{\xi}\right)^{\eta}\right]\right\} \cdot(\sigma_r \tan\varphi_c + c_c) \tag{14}$$

where, ξ and η represent probability parameters in disturbance function; σ_r represents interface normal stress; φ_i and φ_c represent interface friction angle in RI and FA states, respectively; c_i and c_c represent interface adhesion in the RI and FA states, respectively.

The RI and FA states are both perfectly ideal. The actual interface mechanical state is situated somewhere between the two extremes mentioned above. Therefore, the value of the real interface adhesion is situated between the values of c_i and c_c, and the real interface friction angle exhibits a same pattern.

In the case of interface normal stress σ_r=0, this model can further be rewritten as:

$$\tau = \exp\left[-\left(\frac{s}{\xi}\right)^{\eta}\right]\cdot\frac{s}{s_{cr}+s}c_i + \left\{1-\exp\left[-\left(\frac{s}{\xi}\right)^{\eta}\right]\right\}c_c \tag{15}$$

The anchors will be inevitably subjected to some extreme loading conditions during their period of service, such as cyclic loads. From the perspective of loading duration, the cyclic loads and other extreme loads can be deemed as disturbances on the soil-anchor interface. Therefore, the effect of extreme loading conditions on the interface behavior may be described through the modification of the disturbance function.

The applicability and validity of the DSC-based interface model had been verified in previous works through comparing the measurements obtained from direct shear test and element pullout test with the predictions [30]. Hence, this model would be employed in the load-transfer analysis of LDCA.

3.4. Numerical solutions for the load-transfer governing equation

The governing equation can be expressed as the following form by substituting Eq. (14) into Eq. (10).

$$\frac{d^2 s_i(x_i)}{dx_i^2} + \phi(\sigma_{ai})\left[\left(1-D\right)\frac{s_i(x_i)\tan\varphi_i}{s_{cr}+s_i(x_i)} + D\tan\varphi_c\right]\sigma_{ri}(x_i) + \phi(\sigma_{ai})\left[\left(1-D\right)\frac{s_i(x_i)c_i}{s_{cr}+s_i(x_i)} + Dc_c\right] = 0 \tag{16}$$

where, $\phi(\sigma_{ai}) = \frac{\mu_p}{E_g A_g}\left[2\nu_g\frac{df(\sigma_{ai})}{d\sigma_{ai}} - 1\right]$; $D = 1 - \exp\left[-\left(\frac{s}{\xi}\right)^{\eta}\right]$.

σ_{ri} was denoted by s_i to reduce the number of variables in Eq. (16). Combining Eqs. (4), (7), and (8), the relationship between σ_{ri} and s_i can be established as:

$$\sigma_{ri}(x_i) = \begin{cases} 0, \sigma_{ai}(x_i) < 0 \\ \dfrac{kE_g}{2k\nu_g - 1}\cdot\dfrac{ds_i(x_i)}{dx_i}, \sigma_{ai}(x_i) \geq 0 \end{cases} \tag{17}$$

The load-transfer governing equation in its final form can be derived by substituting Eqs. (7) and (17) into Eq. (16), as shown in Eq. (18).

$$\frac{d^2 s_i(x_i)}{dx_i^2} + \frac{\mu_p \xi k}{A_g}\left[(1-D)\frac{s_i(x_i)\tan\varphi_i}{s_{cr}+s_i(x_i)} + D\tan\varphi_c\right]\frac{ds_i(x_i)}{dx_i} + \frac{\mu_p}{E_g A_g}\left(2\xi k\nu_g - 1\right)\left[(1-D)\frac{s_i(x_i)c_i}{s_{cr}+s_i(x_i)} + Dc_c\right] = 0 \tag{18}$$

where, ξ is a factor that distinguishes whether the anchor body is tensioned or compressed, $\xi = \begin{cases} 0, \sigma_{ai}(x_i) < 0 \text{ or } s_i(x_i) < s_i(x_{i+1}) \\ 1, \sigma_{ai}(x_i) \geq 0 \text{ or } s_i(x_i) \geq s_i(x_{i+1}) \end{cases}$.

The load-transfer governing equation is a second-order nonlinear

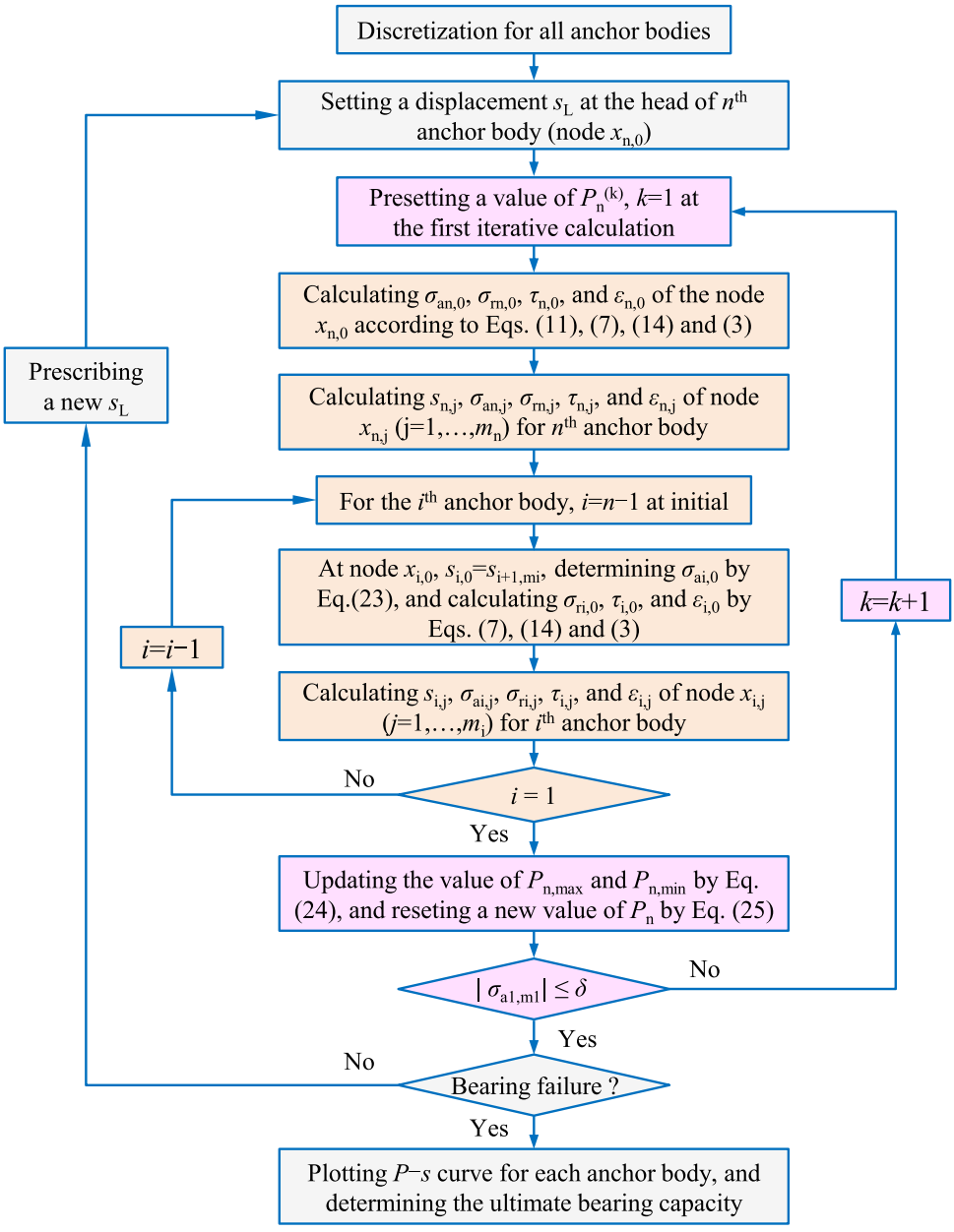

Fig. 6. Flow chart for deriving the numerical solutions.

differential equation, and its closed-form solution is extremely hard to obtain. Therefore, this study utilized the finite difference method to deduce the numerical solutions of Eq. (18). The program for solving this problem was illustrated in Fig. 6, and the details were described below.

Step 1: The i^{th} anchor body is uniformly divided into m_i units along the axial direction. The length of each unit ΔL_i is equal to L_{ai}/m_i. The m_i+1 nodes are numbered from the head of i^{th} bearing plate to the end of i-1th bearing plate, and named $x_{i,0}$, $x_{i,1}$, $x_{i,2}$, …, $x_{i,mi}$ in order, as shown in Fig. 7.

Step 2: The pullout load is applied by displacement-controlled method aiming at capturing the accurate load–displacement curve, in particular for the stage after reaching the ultimate pullout load. The n^{th} anchor body that is located at the end of the LDCA is selected and analyzed at first. The head of n^{th} anchor body (node $x_{n,0}$) is prescribed

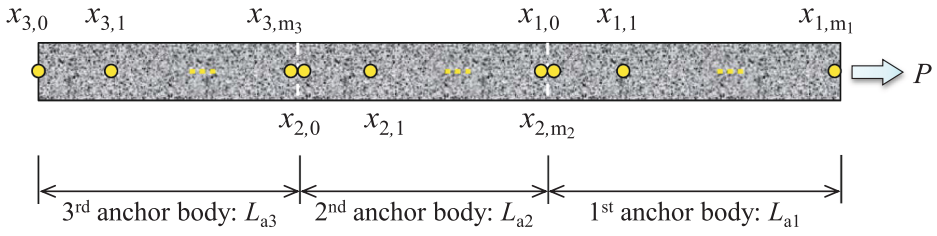

Fig. 7. The node division of anchor bodies.

with a pullout displacement s_L.

Step 3: The axial stress for each anchor body can merely be calculated by iteration method. Preset a value of the compressive force $P_n^{(1)}$ acting on the n^{th} bearing body. Hereinto, the superscript denotes the number of iterative calculations. For the n^{th} anchor body at node $x_{n,0}$, the interface shear displacement $s_{n,0}$=s_L, and the axial stress $\sigma_{an,0}$ can be calculated by Eq. (11). Then Eqs. (7), (14), and (3) are utilized successively to calculate the interface normal stress $\sigma_{rn,0}$, interface shear stress $\tau_{n,0}$, and axial strain $\varepsilon_{n,0}$.

Step 4: For node $x_{n,1}$, its interface shear stress $s_{n,1}$ can be calculated by the differential form of Eq. (8), which is expressed as Eq. (19).

$$s_{n,1} = s_{n,0} - \varepsilon_{n,0} \cdot \Delta L_n \tag{19}$$

The axial stress at this node $\sigma_{an,1}$ can be obtained based on the difference form of Eq. (10), as shown below.

$$\sigma_{an,1} = \sigma_{an,0} - \frac{u_p \Delta L_n}{A_g} \tau_{an,0} \tag{20}$$

The interface normal stress $\sigma_{rn,1}$, interface shear stress $\tau_{n,1}$, and axial strain $\varepsilon_{n,1}$ can be determined by Eqs. (7), (14), and (3) in sequence.

Step 5: The difference form of load-transfer governing equation (Eq. 16) is expressed as:

$$\begin{aligned} &\frac{s_{n,2} - 2s_{n,1} + s_{n,0}}{{\Delta L_n}^2} + \frac{\mu_p \xi k}{A_g}\left[(1-D)\frac{s_{n,1}\tan\varphi_i}{s_{cr}+s_{n,1}} + D\tan\varphi_c\right]\frac{s_{n,1} - s_{n,0}}{\Delta L_n} \\ &+ \frac{\mu_p}{E_g A_g}\left(2\xi k \nu_g - 1\right)\left[(1-D)\frac{s_{n,1}c_i}{s_{cr}+s_{n,1}} + Dc_c\right] \\ &= 0 \end{aligned} \tag{21}$$

The interface shear displacement at node $x_{n,2}$ can be obtained by rewriting Eq. (21).

$$\begin{aligned} s_{n,2} = {} & 2s_{n,1} - s_{n,0} - \frac{\mu_p \xi k}{A_g}\left[(1-D)\frac{s_{n,1}\tan\varphi_i}{s_{cr}+s_{n,1}} + D\tan\varphi_c\right]\left(s_{n,1} - s_{n,0}\right)\Delta L_n \\ & - \frac{\mu_p}{E_g A_g}\left(2\xi k \nu_g - 1\right)\left[(1-D)\frac{s_{n,1}c_i}{s_{cr}+s_{n,1}} + Dc_c\right]{\Delta L_n}^2 \end{aligned} \tag{22}$$

The axial stress $\sigma_{an,2}$, interface normal stress $\sigma_{rn,2}$, interface shear stress $\tau_{n,2}$, and axial strain $\varepsilon_{n,2}$ at node $x_{n,2}$ can further be calculated. Analogously, $s_{n,2}$, $\sigma_{an,j}$, $\sigma_{rn,j}$, $\tau_{n,j}$, and $\varepsilon_{n,j}$ for the n^{th} anchor body at node $x_{n,j}$ (j=3,…,m_n) are also determined by repeating this step.

Step 6: According to assumption (c), the interface shear displacement at node $x_{n\text{-}1,0}$ for the n-1th anchor body is equal to that of node $x_{n,mn}$ for the n^{th} anchor body. That is, $s_{n\text{-}1,0}$=$s_{n,mn}$. An abrupt change of axial stress for the anchor body occurred at the n-1th bearing plate owing to the application of compressive force $P_{n\text{-}1}$. The axial stress at node $x_{n\text{-}1,0}$ can be determined by using Eq. (12), which is equal to:

$$\sigma_{a(n-1),0} = \frac{P_{n-1}}{A_g} - \sigma_{an,m_n} \tag{23}$$

The change of axial stress results in the change of interface normal stress, interface shear stress, and axial strain at the n-1th bearing plate. The values of $\sigma_{r(n\text{-}1),0}$, $\tau_{n\text{-}1,0}$ and $\varepsilon_{n\text{-}1,0}$ at node $x_{n\text{-}1,0}$ can be calculated by Eqs. (7), (14), and (3), respectively. With regard to steps 4 and 5, the interface shear displacements, axial stresses, interface normal stresses, and interface shear stresses at the other nodes $x_{n\text{-}1,j}$ (j=1,…,$m_{n\text{-}1}$) of the n-1th anchor body are obtained successively.

Step 7: Referring to steps 3–6, the interface shear displacements, axial stresses, interface normal stresses, and interface shear stresses for the other anchor bodies can further be calculated.

Step 8: As described in Eq. (11), the axial stress for node $x_{1,m1}$ of 1st anchor body is equal to zero. It serves as a control condition for iterative computation. The iterative calculation error is prescribed to be δ. The iterative calculation will continue until the calculation accuracy of axial stress $\sigma_{a1,m1}$ reaches the preestablished error. This process is actually finding a unique value for compressive force P_n that can correspond to the prescribed pullout displacement s_L at the end of anchorage segment. To achieve this, Eq. (24) is especially established.

$$\begin{cases} P_{n,max} = P_n^{(1)},\ P_{n,min} = 0 & \text{if } \sigma_{a1,m_1} > \delta \\ P_{n,max} = 2P_n^{(1)},\ P_{n,min} = P_n^{(1)} & \text{if } \sigma_{a1,m_1} < -\delta \end{cases} \tag{24}$$

According to the dichotomy, P_n is reset as:

$$P_n^{(2)} = \frac{P_{n,\,max} + P_{n,\,min}}{2} \tag{25}$$

Steps 3 through 8 are repeated until the desired calculation accuracy is achieved in subsequent iterations.

Step 9: A new value of pullout displacement s_L is selected, and then steps 2 through 8 are repeated to calculate the distributions of interface shear displacement, axial stress, and interface shear stress of LDCA under various pullout displacements or pullout loads.

Step 10: The pullout displacement S_i of unbonded steel strand connected with the i^{th} bearing body is the sum of the interface shear displacement $s_{i,0}$ at node $x_{i,0}$ and the tensile deformation Δ_i. The relationship can be described by Eq. (26).

$$S_i = s_{i,0} + \Delta_i = s_{i,0} + \frac{P_i}{E_b A_b}\left(L_f + \sum_{j=1}^{i} L_{aj}\right) \tag{26}$$

where, E_b and A_b represent Young's modulus and cross-sectional area of the unbonded steel strand, respectively; L_f represents the free length of LDCA; L_{aj} represents the length of j^{th} anchor body.

A theoretical model for analyzing the load-transfer behaviors of LDCA was developed by executing the above procedures. This model can be employed to calculate the stress distribution over anchorage segment and the load-displacement curve for each anchor body or unbonded steel strand. The ultimate bearing capacity of LDCA is equal to the maximum value of the sum of the compressive forces subjected to all bearing plates. Noteworthy that all anchor bodies were assumed to be a whole and did not disengage in this theoretical framework. Hence, the model will be not available if the tensile stress exceeds the tensile strength of anchor body.

The employment of finite difference method in this theoretical framework offers the potential for analyzing the load-transfer behaviors of LDCA under various geotechnical conditions, such as layer soils. The following two points should be considered if the developed theoretical model is adopted in some complicated geological conditions: (a) The parameters of the DSC-based model used to characterize the interface nonlinear behaviors between the anchor and each type of soil should first be obtained as well as the surrounding soil's mechanical parameters, including Young's modulus and Poisson's ratio; (b) The segmented analysis for the anchors is conducted based on the soil distribution and the anchor body layout. Noteworthy that the interface model parameters and the mechanical parameters corresponding to each type of soil need to be substituted into the proposed theoretical framework in this process.

Although the developed load-transfer theoretical model is applicable only to short-term loads, it can also provide insights for the analysis of LDCAs under various loading conditions. Specifically, it needs to integrate the interface model and the material models that are compatible with the investigated loading conditions into this theoretical framework. For instance, rheological models are indispensable to characterize the creep behaviors of the soil-anchor interface and the anchor body; dynamic models may be required for cyclic or seismic loading conditions. Noteworthy that the load-transfer governing equation of LDCAs may be hard to explicitly formulate in this case, and the implementation of novel methodologies is needed.

4. Finite element simulations for verification of the theoretical model

4.1. Geometric dimension, mesh generation and model parameters

Three groups of three-dimensional finite element models are established in ABAQUS to simulate the load-transfer behavior of LDCA. As the cases of theoretical model verification, these three FE models of LDCA are designed with 1, 2, and 3 anchor bodies respectively, among which the anchor equipped with only one anchor body is virtually the load-concentrated compression anchor (LCCA). The anchorage segments are all 12 m in total length. The anchor diameters are all 130 mm. The anchor bodies are 12 m, 6 m, and 4 m in length for the three groups of LDCA, respectively. The reinforcement bar is 36 mm in diameter. The LDCA exhibits axisymmetric features in geometry and mechanics. Therefore, all 3D FE models of LDCAs are developed with 1/2 scale for improving the simulation efficiency. Geometric dimension and boundary conditions of the FE models are shown in Fig. 8. Proportional coefficient α_i is stipulated to be 1.0, which implies the compressive force exerted on each anchor body is equal. Young's modulus and Poisson's ratio of the anchor body are 30 GPa and 0.22, respectively. The surrounding soil is homogeneous and equipped with high strength. Young's modulus and Poisson's ratio of the soil are 200 MPa and 0.33, respectively. All parts were made up of C3D8R elements. The steps of FE simulation were programmed according to the bearing characteristics and the construction technology of LDCA, including ground stress balance, anchor hole creation, anchor-soil contact, and pullout load application [33,34].

The cohesive contact elements were employed to characterize the nonlinear interface behaviors between soil and anchor in the present FE simulation. Hereinto, the interface damage evolution was stipulated in exponential form [35,36]. The interface model parameters are defined as: interface elastic shear stiffness k_c=8.5×10^4 kPa.m^{-1}, initiation slip at bond damage s_c^b=1.6 mm, ultimate interface cohesive stress τ_c^b=136 kPa, displacement at complete failure s_c^u=30 mm, and damage evolution rate α=2.8. Noteworthy that the interface mechanical model used in FE

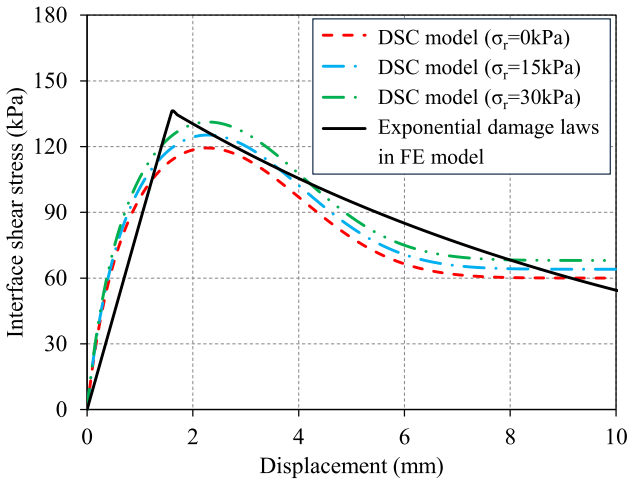

Fig. 9. Comparisons of the characterization for soil-anchor interface behavior between FE simulation and theoretical modeling.

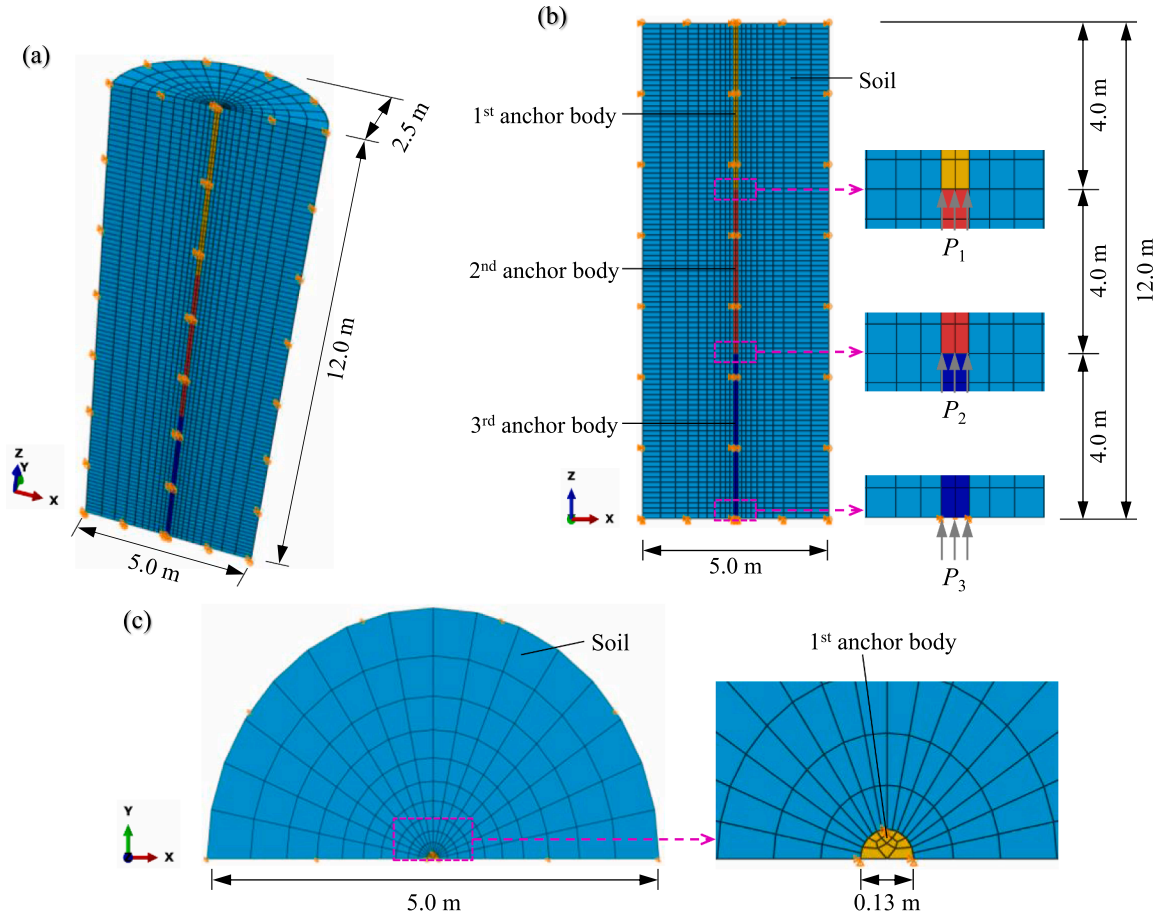

Fig. 8. Geometric dimension, mesh generation and boundary conditions of the FE model for LDCA equipped with three anchor bodies: (a) three-dimensional view; (b) front view; (c) top view.

simulation is different from that used in the above theoretical analysis. Therefore, it is extremely crucial to ensure the consistency of the soil-anchor interface mechanical behaviors defined in FE simulation and theoretical analysis. Based on the least square method, Eq. (14) was utilized to fit the interface shear stress-displacement curve concretized by the exponential damage interface model. The result of regression analysis was illustrated in Fig. 9. All parameters of the DSC-based interface non-linear model were further obtained, including s_{cr}=0.8 mm, ξ=4.2, η=2.8, φ_i=32°, c_i=180 kPa, φ_c=16°, c_c=60 kPa. More details about the definitions of the five interface model parameters in FE simulation as well as the calibration for the theoretical model parameters can be found in Zhu et al. [30,37].

4.2. Numerical verification for the load-transfer theoretical model

Fig. 10 compares the pullout load *P*- displacement *s* curves for LDCAs equipped with different numbers of anchor bodies obtained from FE simulation and theoretical analysis. The three groups of theoretically calculated *P-s* curves were all in good agreement with the numerical simulation results. Table 1 summarizes the relative errors between FE simulations and theoretical calculations for the ultimate pullout load P_u and the maximum pullout displacement $s_{0,max}$. For these three groups of LDCAs, the relative error of ultimate pullout load obtained from the two methods is no more than 3.5 %, and the relative error of maximum pullout displacement is no more than 5.0 %. Meanwhile, compared with load-concentrated compression anchor (LCCA), the LDCA has larger bearing capacity and smaller displacement. The bearing performance of LDCA improves as the number of anchor bodies increases. For example, the ultimate bearing capacity of the LDCA with three anchor bodies is 11.7 % higher than that of LCCA, and the maximum pullout displacement is 61.3 % smaller.

Table 1
Relative errors between FE simulations and theoretical calculations for ultimate pullout load and maximum pullout displacement.

The number of anchor bodies	Ultimate pullout load P_u			Maximum pullout displacement $s_{0,max}$		
	FEM (kN)	Theory (kN)	Relative error (%)	FEM (mm)	Theory (mm)	Relative error (%)
N_{ac}=1	519.6	501.3	3.5	58.4	56.1	3.9
N_{ac}=2	555.8	547.2	1.5	31.9	30.3	5.0
N_{ac}=3	580.5	574.2	1.1	22.8	21.7	4.8

When the anchor head is exposed to the maximum load, the interface shear displacements along the entire anchorage length range from 1.0 mm to 9.2 mm, 1.0 mm to 4.8 mm, and 1.1 mm to 3.9 mm for the LDCAs comprising one, two, and three anchor bodies, respectively. Noteworthy that the interface shear displacement is different from the pullout displacement given in Table 1. The relationship between these two parameters was expressed by Eq. (26). As shown in Fig. 9, the interface shear stress of the exponential damage laws employed in FE simulation is larger when the displacement ranges from 1.0 mm to 9.2 mm. As a consequence, the ultimate pullout load obtained from FE simulation is larger than that obtained from theoretical calculation. The range of interface shear displacement is larger for the LDCA with fewer anchor bodies, resulting in a greater difference in interface shear stress for these two methods. This is expected to explain why the relative error between FE simulations and theoretical calculations for ultimate pullout load is greater for this LDCA. In addition, a greater pullout load results in

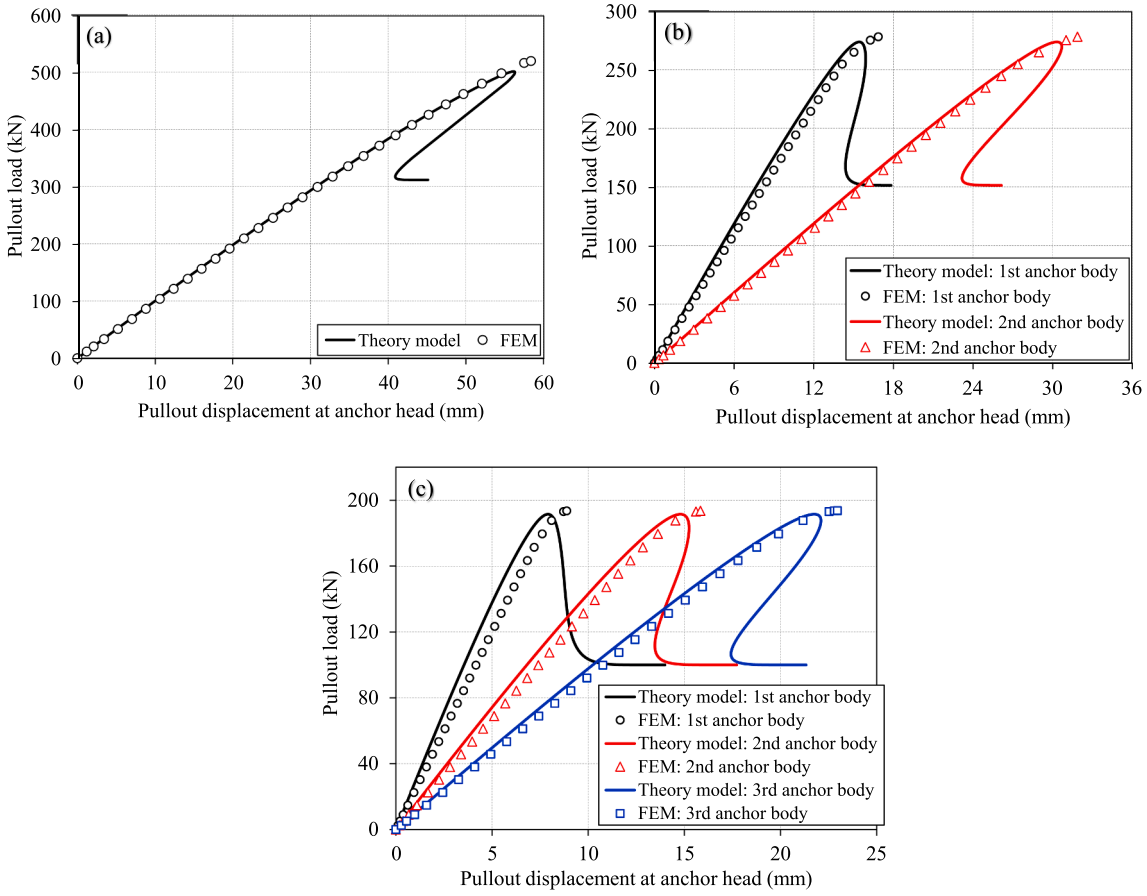

Fig. 10. Comparisons of *P-s* curves for LDCAs obtained from FE simulation and theoretical analysis: (a) one anchor body (that is actually LCCA); (b) two anchor bodies; (c) three anchor bodies.

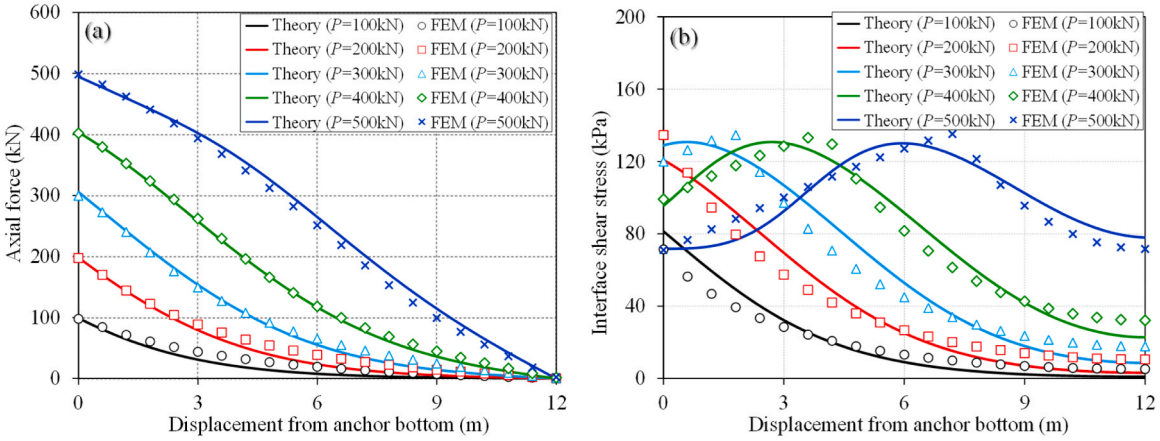

Fig. 11. Comparisons of stress distribution for LDCA with one anchor body obtained from FE simulation and theoretical analysis: (a) axial force; (b) interface shear stress.

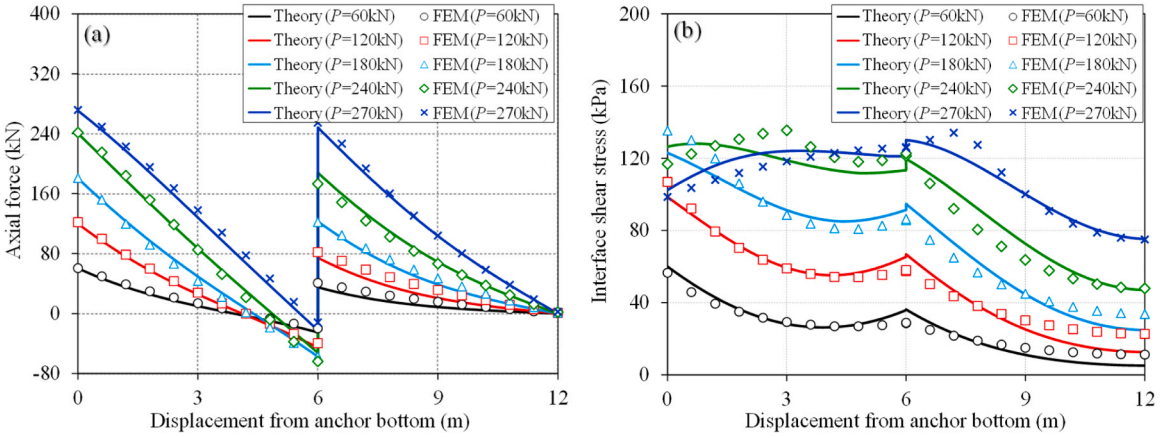

Fig. 12. Comparisons of stress distribution for LDCA with two anchor bodies obtained from FE simulation and theoretical analysis: (a) axial force; (b) interface shear stress.

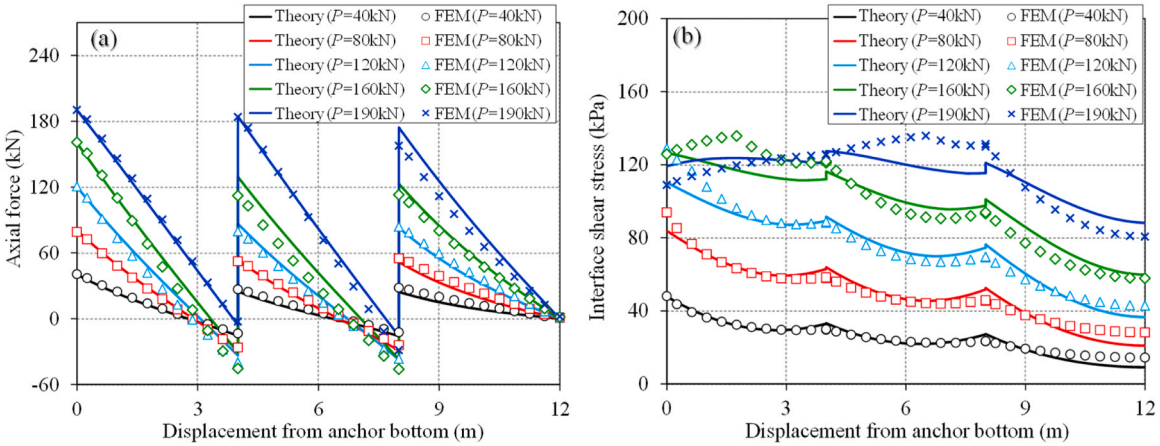

Fig. 13. Comparisons of stress distribution for LDCA with three anchor bodies obtained from FE simulation and theoretical analysis: (a) axial force; (b) interface shear stress.

a greater tensile deformation of the unbonded steel strand, which in turn produces larger pullout displacement for LDCAs in FE simulation.

Figs. 11, 12, and 13 illustrate the distributions of axial force and interface shear stress for LDCAs with different numbers of anchor bodies, as derived from FE simulation and theoretical analysis. Some discrepancies still persist between the results of FE simulations and theoretical calculations when the pullout load is relatively small. This discrepancy can be attributed to the fact that the two interface mechanical models exhibit relatively obvious differences when the interface shear stress is small, in particular below 120 kPa, as shown in Fig. 9.

The differences become more evident between the results yielded by the two methods with the increasing the pullout load. But in general, the theoretically calculated distribution curves of axial force and interface shear stress under various load levels all match well with the FE numerical results. It validates the effectiveness and accuracy of the developed theoretical model in predicting the load-transfer behavior of LDCA.

As shown in Fig. 11, the axial force of LDCA with one anchor body (LCCA) distributed non-linearly over anchorage segment, and the interface shear stress distributed unevenly. However, with the increase of anchor body, the axial force distribution of LDCA tends to be linear and the interface shear stress distribution becomes more uniform. The interface shear strength at different positions can easily be mobilized together for the LDCA with more anchor bodies. Load concentration can also be avoided in this way. This is contributed to the greater bearing capacity for LDCA. The axial force for each anchor body is maximum at its head and is minimum at its end. At the junction of different anchor bodies, the axial force changes abruptly due to the application of compressive force (Figs. 12a and 13a). In the present cases, the anchor bodies are compressed at their heads and are tensioned at their ends, which is described by Eq. (12). The value and distribution area of tensile stress enlarge as the increase of compressive force. The sum of compressive stress and tensile stress of anchor body at this junction is equal to the compressive force exerted on the bearing plate. In addition, as demonstrated in Figs. 12(b) and 13(b), the abrupt alteration of axial force leads to a corresponding change in interface normal stress, which further results in the sudden change of interface shear stress at the junction. The greater the compressive force, the more pronounced the magnitude of the abrupt change in interface shear stress.

5. Verifications through in-situ pullout tests

5.1. Case 1

Shin et al. [23] carried out in-situ pullout tests on LDCAs embedded in weathered rock with varying numbers of anchor bodies. In this study, the experimental data collected from groups T21 and T31 were utilized to validate the proposed theoretical load-transfer model. The LDCAs were designed with two and three anchor bodies, respectively. Besides, they were 105 mm in borehole diameter, 17 m in total anchorage length, 1 m in space of anchor bodies, and 0.4 m in bearing body length. The mechanical parameters of the anchor body and surrounding rock were summarized as: E_g=17.4 GPa, ν_g=0.20, E_s=300 MPa, and ν_s=0.30. The compressive force exerted on each anchor body is 167 kN, and the corresponding proportional coefficient α_i is 1.0. The axial force distributions of LDCAs in the in-situ pullout tests have been discussed through FE simulation by Shin et al. [25]. The parameters of the DSC-based interface model were determined according to the mechanical properties of the surrounding soil and the in-situ pullout test results, including s_{cr}=1.6 mm, ξ=2.2, η=1.8, φ_i=28°, c_i=960 kPa, φ_c=12° and c_c=240 kPa.

Fig. 14 compares the axial force distributions for the two groups of LDCAs obtained from three methods. The theoretical calculations show close match with the in-situ pullout test results and FE simulations. It can be observed that the axial force exhibits markedly nonlinear distribution over anchoring area, and its decrease rate is very fast. In the two cases, for the 1st anchor body, the axial force decreases approximately to zero at 6–8 m from the bottom of anchorage segment. While for the other anchor bodies, the axial force decreases approximately to zero at their ends. The excellent properties of the soil around the anchor and the large soil-anchor interface shear strength contribute to the rapid dissipation of axial force.

5.2. Case 2

Ye et al. [38] carried out in-situ pullout tests for LDCAs used in slope engineering. The LDCA was 200 mm in anchor diameter, and 32 m in total length, of which the anchorage length was 18 m. Four anchor bodies were installed with space of 4.5 m. The anchorage segment was mainly embedded in silty clay. The mechanical parameters of anchor body and surrounding soil were summarized as: $f_{cu,g}$=37 MPa, E_g=20 GPa, ν_g=0.20, E_s=200 MPa, and ν_s=0.33. In order to measure the axial force distribution, sixteen groups of vibrating wire extensometers

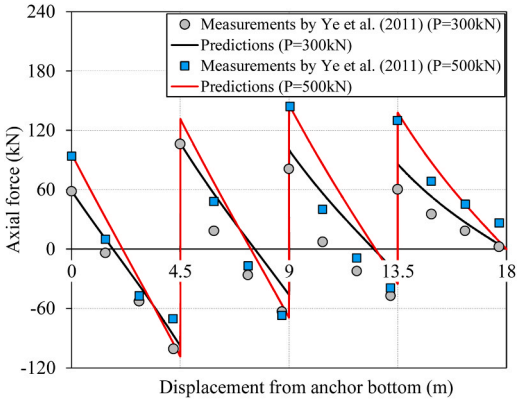

Fig. 15. Comparisons of axial force distribution obtained from in-situ pullout tests and theoretical calculations.

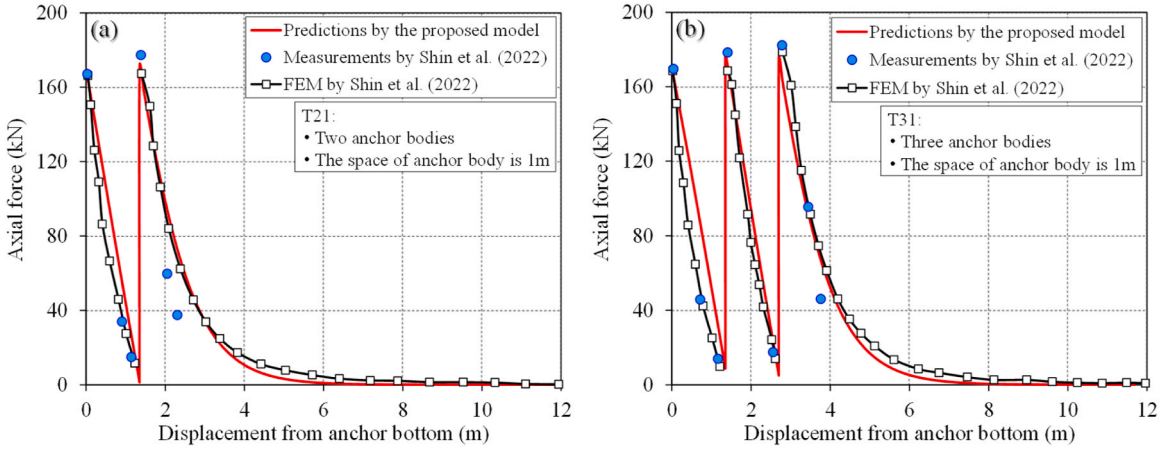

Fig. 14. Comparisons of axial force distribution obtained from in-situ pullout tests, FE simulations and theoretical calculations: (a) T21 (two anchor bodies); (b) T31 (three anchor bodies).

were arranged uniformly along the entire anchorage segment. The testing data with total pullout loads of 300 kN and 500 kN were adopted for theoretical model verification. The parameters of the DSC-based interface model were determined according to the mechanical properties of the surrounding soil and the in-situ pullout test results, including s_{cr}=2.0 mm, ξ=2.8, η=1.8, φ_i=28°, c_i=180 kPa, φ_c=12° and c_c=60 kPa.

Fig. 15 illustrates the comparison between the theoretically predicted axial force distribution and the testing data. Once more, the concordance of the results yielded by the two methods is excellent in this study case. These findings suggest that the theoretical model developed in Section 3 is capable of predicting the load-transfer behavior of the LDCA. Furthermore, unlike the cases in Sub-Section 5.1, the axial force distributes linearly over anchoring area, and the anchor bodies are in tension state in this case. There are two reasons for this phenomenon: (a) the surrounding soil is equipped with suboptimal mechanical performance, resulting in the relatively small soil-anchor interface shear strength; (b) each anchor body is of considerable length.

6. Parametric studies

The effectiveness and accuracy of the developed theoretical model have been examined through FE simulations and in-situ pullout test results. The objective here is to investigate the effects of several key design parameters on the bearing capacity of LDCA. The mechanical parameters of the anchor body, soil, and interface defined in Sub-Section 4.1 served as the baseline in the subsequent discussions.

6.1. Effect of anchorage length

Fig. 16 plotted the relationship between ultimate pullout load and anchorage length for LDCAs with various numbers of anchor bodies. As with the conventional tension anchors, the bearing capacity of LDCA increases in tandem with anchorage length L_a, albeit at a gradually diminishing rate of change. In instances where the anchorage length exceeds 12 m, the increase amplitude of bearing capacity decreases significantly for the LDCAs with single or double anchor bodies. This finding indicates that the length in question is in proximity to the effective anchorage length.

The quantity of anchor bodies also exerts a significant influence on the bearing capacity of LDCA. As shown in Fig. 17, if the anchorage length is relatively brief, measuring less than 6 m, the number of anchor bodies exhibits a negligible impact on the bearing capacity of LDCA. Meanwhile, if the anchorage length is of considerable magnitude, the bearing capacity of LDCAs will be markedly improved with the increase

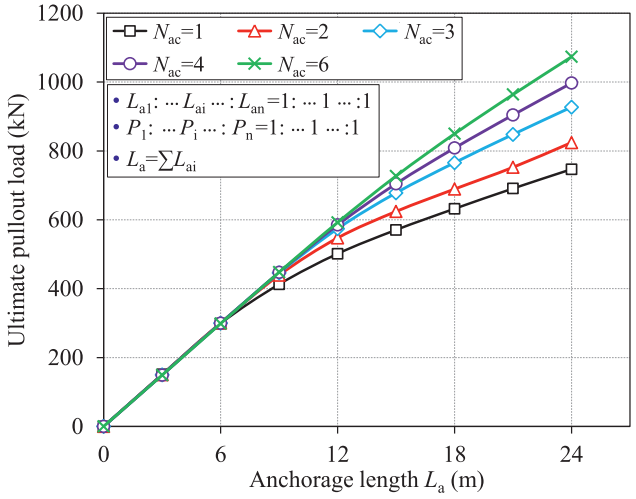

Fig. 16. Relationship between ultimate pullout load and anchorage length for LDCAs with various numbers of anchor bodies.

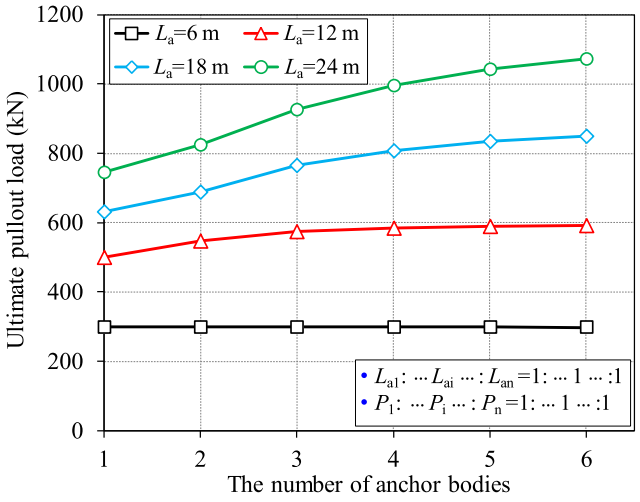

Fig. 17. The influence of the number of anchor bodies on the ultimate pullout load of LDCAs with different anchorage lengths.

of anchor bodies. Therefore, it is an effective method for the bearing performance enhancement of LDCA by increasing the anchorage length and the quantity of anchor bodies. However, the aforementioned strategy does not apply to LCCA.

6.2. Effect of length ratio between different anchor bodies

The LDCA with three anchor bodies was selected as an example to investigate the effect of length ratio between different anchor bodies on the bearing capacity. Fig. 18 illustrates the variation of ultimate pullout load with length ratio for the case of length ratio designed as 1: 1: k. It can be seen that the length ratio between different anchor bodies has minimal impact on the bearing capacity of LDCA if the anchorage length $L_a \leq 12$ m. When the anchorage length $L_a > 12$ m, as the increase of length L_{a3} of the 3rd anchor body, the ultimate pullout load of LDCA will initially increase and then decrease. The maximum bearing capacity is achieved when the length ratio is 1: 1: 2. Hence, the length adjustment for anchor bodies is a reasonable measure for improving the bearing capacity of LDCA, even if the anchorage length and the number of anchor bodies are both constant. There should be an optimal length ratio between different anchor bodies for each LDCA. In other words, the bearing capacity manifests the maximum value for LDCA with this

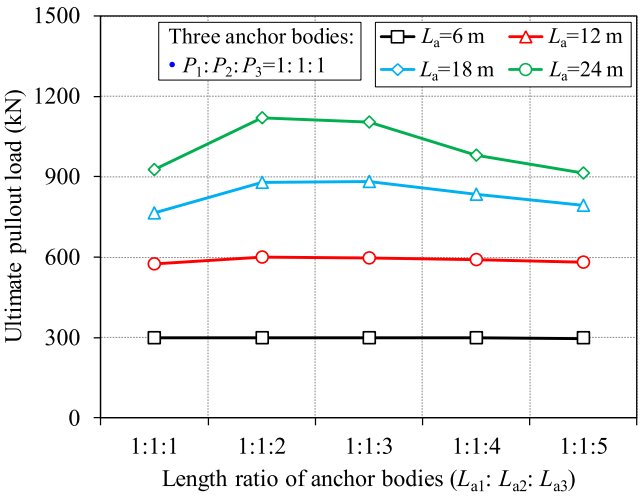

Fig. 18. Effect of length ratio of anchor bodies on the ultimate pullout load for LDCAs with three anchor bodies.

length ratio. The research of optimal length ratio may be relatively easy if the anchor bodies are less in quantity. However, this study will become exceedingly arduous in the event that the LDCA is equipped with numerous anchor bodies, in particular the quantity exceeds three. In this case, the implementation of intelligent optimization methods seems to be beneficial in addressing this issue.

6.3. Effect of load proportional coefficient

Fig. 19 discussed the effect of load proportional coefficient on the ultimate pullout load for LDCAs with three anchor bodies. The length ratio was designed as 1: 1: *k* for the case. The results indicate that load proportional coefficient exhibits a negligible impact on the bearing capacity of LDCA if the anchorage length is relatively brief, in particular less than 6 m. When the anchorage length $L_a \geq 12$ m, the ultimate pullout load of LDCA decreases with the increase of load proportional coefficient. The larger the anchorage length, the more significant the reduction of bearing capacity. Accordingly, if the length of each anchor body is identical, the LDCA will attain its maximum bearing capacity under conditions of equal compressive force on each bearing plate. Another issue to keep in mind is that the interaction exists between length ratio and load proportional coefficient with regard to the bearing capacity of LDCA. It is an exceptionally difficult challenge to ascertain the optimal length ratio and load proportional coefficient simultaneously.

6.4. Effect of axial stiffness

The axial stiffness of anchor body is also an important parameter that affects the bearing performance of LDCA. As illustrated in Fig. 20, an increase in the axial stiffness of the anchor body results in a corresponding enhancement in the bearing capacity of the LDCA, which ultimately attains a specific value. In addition, the less the number of anchor bodies, the greater influence of axial stiffness on the bearing capacity of LDCA. Therefore, in the case of the LDCA equips with few anchor bodies, increasing the axial stiffness of anchor body is a beneficial measure to the improvement of bearing capacity. However, this does not apply to the LDCAs with a large number of anchor bodies.

7. Summary and conclusions

This paper developed a novel method for the load-transfer analysis of LDCA from the theoretical solution perspective. The interface mechanical behavior between soil-anchor was characterized by a DSC-based

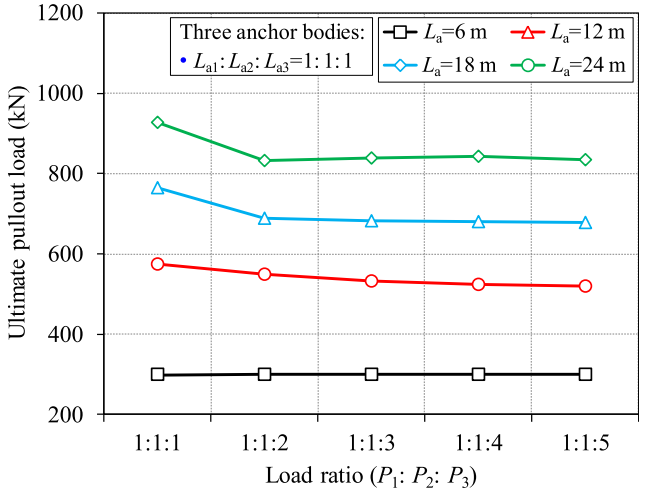

Fig. 19. Effect of load proportional coefficient on ultimate pullout load for LDCAs with three anchor bodies.

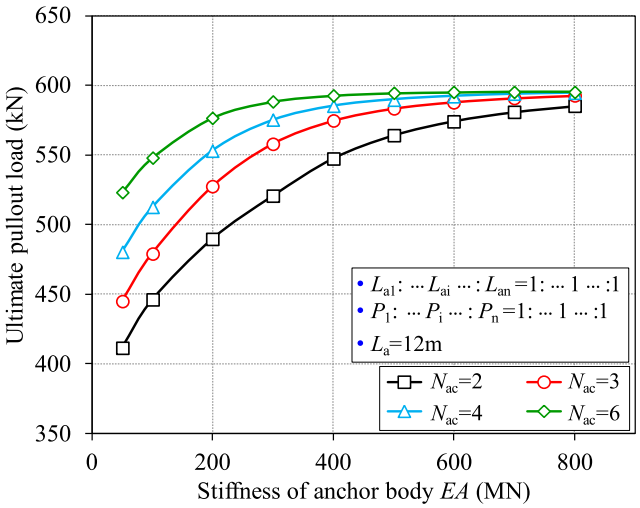

Fig. 20. Calculated ultimate pullout load versus axial stiffness for LDCAs with different numbers of anchor bodies.

nonlinear model. The bearing mechanism of LDCA was subjected to particular consideration through the integration of finite difference method. Three-dimensional finite element models were established to simulate the load-transfer behavior of LDCA with different numbers of anchor bodies. The theoretical calculations were compared with FE numerical results for the verification of the theoretical model. Parametric studies were finally conducted. The main conclusions are summarized as follows.

(1) The load-displacement curves, axial stress, and interface shear stress distributions for LDCAs with different numbers of anchor bodies predicted by the proposed DSC-based theoretical model were all in good agreement with the results from FE simulations and in-situ pullout tests, proving that the theoretical model is deemed efficient and accurate for the prediction of the load-transfer behavior of LDCA.
(2) Compared with the load-concentrated anchor, LDCA exhibits a greater pullout capacity and a smaller displacement. This is due to the fact that the pullout load dispersion serves to eliminate stress concentrations, and the interface shear stress distributes more uniformly.
(3) The distribution of interface shear stress will be more uniform if the LDCAs are equipped with more anchor bodies, which is beneficial to the corporate mobilization of interface shear strength at different positions, so that the anchor can easily obtain better bearing performance.
(4) It is an effective method for the bearing performance enhancement of LDCA through increasing the anchorage length or axial stiffness of anchor body and the quantity of anchor bodies simultaneously.
(5) The interval between adjacent bearing bodies should be designed carefully and be sufficiently large for preventing the occurrence of tensile stress in the anchor bodies.
(6) The length ratio and load proportional coefficient between different anchor bodies will exert a remarkable influence on the load-transfer behavior of LDCA if its anchorage length is large. For LDCAs with three anchor bodies, if the compressive force applied on each bearing plate is identical, the maximum bearing capacity is achieved when the length ratio is 1: 1: 2. Meanwhile, if the length for each anchor body is identical, the maximum bearing capacity is achieved when the load proportional coefficient is 1: 1: 1.

The bearing mechanism of LDCA is considerably more intricate than that of conventional load-concentrated anchor. The bearing performance of LDCA is influenced by a multitude of factors. Hereinto, the interaction exists between the length ratio and load proportional coefficient of different anchor bodies. It is an exceptionally difficult challenge to ascertain the optimal length ratio and load proportional coefficient simultaneously, especially for LDCAs equipped with many anchor bodies. The implementation of intelligent optimization methods, such as surrogate model, may be beneficial in addressing this issue. The optimal parameters obtained through optimization analysis may need to be adjusted according to the real engineering conditions, including construction, environment, materials, etc. This is a systematic work that necessitates the integration of new methodologies or models. The researches in these areas were thus not conducted in this work, but is currently the subject of a new project.

CRediT authorship contribution statement

Shimin Zhu: Writing – original draft, Software, Methodology, Formal analysis, Data curation, Writing – review & editing. **Changfu Chen:** Supervision, Funding acquisition, Conceptualization. **Genbao Zhang:** Writing – original draft, Software. **Mingbin Wang:** Validation, Supervision. **Zhuangwei Zhang:** Data curation.

Declaration of Competing Interest

The authors declare that they have no known competing financial interests or personal relationships that could have appeared to influence the work reported in this paper.

Data availability

Data will be made available on request.

Acknowledgements

This research was sponsored by the National Natural Science Foundation of China (grant number: 52278349). The authors appreciate their financial support.

References

[1] C. Kong, T. Yang, M. Xiao, Q.T. Yuan, Numerical simulation of fully grouted rock bolts with or without faceplates based on the tri-linear bond-slip model, Constr. Build. Mater. 367 (2023) 130288, https://doi.org/10.1016/j.conbuildmat.2022.130288.
[2] C. Li, B. Stillborg, Analytical models for rock bolts, Int. J. Rock Mech. Min. Sci. 36 (8) (1999) 1013–1029, https://doi.org/10.1016/S1365-1609(99)00064-7.
[3] C.F. Chen, S.M. Zhu, G.B. Zhang, F.S. Mao, H. Cai, Time-dependent load transfer behavior of grouted anchors in laterite, Comput. Geotech. 132 (2021) 103969, https://doi.org/10.1016/j.compgeo.2020.103969.
[4] L.B. Martín, M. Tijani, F. Hadj-Hassen, A new analytical solution to the mechanical behaviour of fully grouted rockbolts subjected to pull-out tests, Constr. Build. Mater. 25 (2) (2011) 749–755, https://doi.org/10.1016/j.conbuildmat.2010.07.011.
[5] N.K. Kim, Performance of tension and compression anchors in weathered soil, J. Geotech. Geoenviron. Eng. 129 (12) (2003) 1138–1150, https://doi.org/10.1061/(ASCE)1090-0241(2003)129:12(1138).
[6] W.B. Chen, C.Y. Hong, X.S. Chen, G.B. Luo, D. Su, Comparative analysis of anchor cables in pullout tests using distributed fiber optic sensors, Can. Geotech. J. 60 (2023) 1861–1876, https://doi.org/10.1139/cgj-2022-0455.
[7] H.H. Zhu, J.H. Yin, A.T. Yeung, W. Jin, Field pullout testing and performance evaluation of GFRP soil nails, J. Geotech. Geoenviron. Eng. 137 (7) (2011) 633–642, https://doi.org/10.1061/(ASCE)GT.1943-5606.0000457.
[8] I.W. Farmer, Stress distribution along a resin grouted rock anchor, Int. J. Rock Mech. Min. Sci. Geomech. Abstr. 12 (11) (1975) 347–351, https://doi.org/10.1016/0148-9062(75)90168-0.
[9] C.F. Chen, S.M. Zhu, G.B. Zhang, A.M. Morsy, J.G. Zornberg, F.S. Mao, A generalized load-transfer modelling framework for tensioned anchors integrating adhesion-friction-based interface model, Int. J. Geomech. 22 (5) (2022) 04022036, https://doi.org/10.1061/(ASCE)GM.1943-5622.0002338.
[10] W.L. Zhang, L. Huang, H. Juang, An analytical model for estimating the force and displacement of fully grouted rock bolts, Comput. Geotech. 117 (2020) 103222, https://doi.org/10.1016/j.compgeo.2019.103222.
[11] J.H. Chen, S. Saydam, P.C. Hagan, An analytical model of the load transfer behavior of fully grouted cable bolts, Constr. Build. Mater. 101 (2015) 1006–1015, https://doi.org/10.1016/j.conbuildmat.2015.10.099.
[12] S.Q. Ma, J. Nemcik, N. Aziz, An analytical model of fully grouted rock bolts subjected to tensile load, Constr. Build. Mater. 49 (2013) 519–526, https://doi.org/10.1016/j.conbuildmat.2013.08.084.
[13] F.F. Ren, Z.J. Yang, J.F. Chen, W.W. Chen, An analytical analysis of the full-range behaviour of grouted rockbolts based on a tri-linear bond-slip model, Constr. Build. Mater. 24 (2010) 361–370, https://doi.org/10.1016/j.conbuildmat.2009.08.021.
[14] M.X. Fu, S.S. Huang, K. Fan, S.W. Liu, D.Y. He, H.S. Jia, Study on the relationship between the maximum anchoring force and anchoring length of resin-anchored bolts of hard surrounding rocks based on the main slip interface, Constr. Build. Mater. 409 (2023) 134000, https://doi.org/10.1016/j.conbuildmat.2023.134000.
[15] C.C. Li, Rockbolting: Principles and Applications, Butterworth-Heinemann, Oxford, UK, 2017.
[16] CECS 22, Technical Specification For Ground Anchors, China Planning Press, Beijing, China, 2005.
[17] J.Q. Jia, B.X. Tu, H.T. Wang, G. Meng, D.L. Yao, Mechanical behaviors of pressure-dispersive prestressed anchor, Chin. J. Geotech. Eng. 33 (9) (2011) 1320–1325.
[18] S.C. Hsu, C.M. Chang, Pullout performance of vertical anchors in gravel formation, Eng. Geol. 90 (2007) 17–29, https://doi.org/10.1016/j.enggeo.2006.11.004.
[19] H.J. Liao, C.D. Ou, S.C. Shu, Anchorage behavior of shaft anchors in alluvial soil, J. Geotech. Eng. 122 (7) (1996) 526–533, https://doi.org/10.1061/(ASCE)0733-9410(1996)122:7(526).
[20] S.G. Wu, H.M. Fu, Y.Y. Zhang, Study on anchorage mechanism and application of tension-compression dispersive anchor cable, Rock. Soil Mech. 39 (6) (2018) 2155–2163+2174.
[21] J.S. Tian, L. Hu, Review on the anchoring mechanism and application research of compression-type anchor, Engineering 08 (2016) 777–788, https://doi.org/10.4236/eng.2016.811070.
[22] G.B. Shin, B.H. Jo, S.R. Kim, C.K. Chung, S.H. Baek, Field study on behavior of load distributive compression anchor installed in weathered rock and soft rock, Can. Geotech. J. (2023), https://doi.org/10.1139/cgj-2022-0384.
[23] G.B. Shin, B.H. Jo, S.H. Baek, S.R. Kim, C.K. Chung, Load transfer mechanism of a load distributive compression anchor installed in weathered rock layer, Can. Geotech. J. 59 (2022) 473–484, https://doi.org/10.1139/cgj-2020-0553.
[24] Y.Y. Xia, Z.S. Chen, J.C. Gu, L.L. Zhang, X.Y. Zheng, Indoor full-size model test on stress features of pressure-dispersive prestressed anchorage cable, J. Wuhan. Univ. Technol. 32 (3) (2010) 33–37.
[25] G.B. Shin, B.H. Jo, S.R. Kim, S.H. Baek, C.K. Chung, Numerical simulation of load distributive compression anchor installed in weathered rock layer, Acta Geotech. 17 (2022) 4173–4190, https://doi.org/10.1007/s11440-022-01523-7.
[26] H. Fan, A.P. Vassilopoulos, T. Keller, Load transfer mechanisms in CFRP ground anchors with multi-strap ends, Compos. Struct. 184 (2018) 125–134, https://doi.org/10.1016/j.compstruct.2017.09.111.
[27] N.K. Kim, J.S. Park, S.K. Kim, Numerical simulation of ground anchors, Comput. Geotech. 34 (2007) 498–507, https://doi.org/10.1016/j.compgeo.2006.09.002.
[28] R. Rui, Y.Y. Xia, J.C. Gu, C. Chen, Non-uniform shear stress design method for pressure-dispersive anchors, Chin. J. Geotech. Eng. 34 (7) (2012) 1262–1270.
[29] J.Q. He, L. Wang, Q.N. Chen, Study on Load-transfer mechanism of anchorage segment of pressure-type anchor. Chin, J. Appl. Mech. 30 (6) (2013) 864–869. DOI: 10.11776/cjam.30.06.B023.
[30] S.M. Zhu, C.F. Chen, F.S. Mao, H. Cai, Application of disturbed state concept for load-transfer modeling of recoverable anchors in layer soils, Comput. Geotech. 137 (2021) 104292, https://doi.org/10.1016/j.compgeo.2021.104292.
[31] C.S. Desai, Y. Ma, Modeling of joints and interfaces using the disturbed-state concept. Int. J. Numer. Anal. Methods Geomech. 16 (9) (1992) 623–653.
[32] E.G. Baghini, M.M. Toufigh, V. Toufigh, Analysis of pile foundations using natural element method with disturbed state concept, Comput. Geotech. 96 (2018) 178–188, https://doi.org/10.1016/j.compgeo.2017.11.005.
[33] W.H. Zhou, J.H. Yin, C.Y. Hong, Finite element modeling of pullout testing on a soil nail in a pullout box under different overburden and grouting pressures, Can. Geotech. J. 48 (2011) 557–567, https://doi.org/10.1139/t10-086.
[34] X.Y. Ye, S.Y. Wang, X. Xiao, S. Sloan, D.C. Sheng, Numerical study for compaction-grouted soil nails with multiple grout bulbs, Int. J. Geomech. 19 (2) (2019) 04018193, https://doi.org/10.1061/(ASCE)GM.1943-5622.0001342.
[35] S.S. Yu, W.C. Zhu, L.L. Niu, S.C. Zhou, P.H. Kang, Experimental and numerical analysis of fully grouted long rockbolt load-transfer behavior, Tunn. Undergr. Space Technol. 85 (2019) 56–66, https://doi.org/10.1016/j.tust.2018.12.001.
[36] M. Rezazadeh, V. Carvelli, A. Veljkovic, Modeling bond of GFRP rebar and concrete, Constr. Build. Mater. 153 (2017) 102–116, https://doi.org/10.1016/j.conbuildmat.2017.07.092.
[37] S.M. Zhu, C.F. Chen, H. Cai, F.S. Mao, Analytical modeling for the load-transfer behavior of stiffened deep cement mixing (SDCM) pile with rigid cap in layer soils, Comput. Geotech. 144 (2022) 104618, https://doi.org/10.1016/j.compgeo.2021.104618.
[38] G.B. Ye, Z.Y. He, Y.B. Gao, D.M. Ma, W.T. Zhong, Field test study of load distribution of anchoring section of pressure dispersed anchor cables, Rock. Soil Mech. 32 (12) (2011) 3561–3565.